Ferret Thoracic Anatomy by 2-Deoxy-2-(18F)Fluoro-D-Glucose (18F-FDG) Positron Emission Tomography/Computed Tomography (18F-FDG PET/CT) Imaging

Albert Wu, Huaiyu Zheng, Jennifer Kraenzle, Ashley Biller, Carol D. Vanover, Mary Proctor, Leslie Sherwood, Marlene Steffen, Chin Ng, Daniel J. Mollura, and Colleen B. Jonsson

Albert Wu, BA, is a Medical Student and Clinical Research Training Program (CRTP) Participant at the Center for Infectious Disease Imaging (CIDI), Department of Radiology and Imaging Sciences, National Institutes of Health, Bethesda, MD. The following eight authors hold positions at the University of Louisville, Center for Predictive Medicine, Louisville, KY: Huaiyu Zheng, MD, is a Research Associate, Department of Radiology; Jennifer Kraenzle, RLATg, is the Vivarium Assistant Manager in the Center for Predictive Medicine; Ashley Biller, LVT, LAT, is a Vivarium Senior Husbandry Technician in the Center for Predictive Medicine; Carol D. Vanover, RLAT, Vivarium Manager in the Center for Predictive Medicine; Mary Proctor, DVM, MS, DACLAM, is Associate Director and Assistant Professor in the Department of Research Resources Facilities; Leslie Sherwood, DVM, is Staff Veterinarian and Assistant Professor in the Department of Research Resources Facilities; Marlene Steffen, BS, is the Facilities Operations Manager at the Center for Predictive Medicine; and Chin Ng, PhD, is an Associate Professor, Department of Radiology. Daniel J. Mollura, MD, is the Deputy Director and Staff Clinician/Radiologist at the Center for Infectious Disease Imaging (CIDI), Department of Radiology and Imaging Sciences, National Institutes of Health, Bethesda, MD. Colleen B. Jonsson, PhD, is the Director of the Center for Predictive Medicine at the University of Louisville.

Address correspondence and reprint requests to Daniel J. Mollura, MD, Center for Infectious Disease Imaging, Department of Radiology and Imaging Sciences, National Institutes of Health, 10 Center Drive, Building 10, 1C349, (Mailstop 1182), Bethesda, MD 20892, email molluradj@cc.nih.gov; OR to Colleen B. Jonsson, PhD, Clinical and Translational Research Building, 6th Floor, 505 South Hancock St., Louisville, KY 40202, email cbjons01@louisville.edu.

Abbreviations that appear ≥3× throughout this article: ^{18}F-FDG, 2-deoxy-2-(^{18}F)fluoro-D-glucose; CT, computed tomography; ELISA, enzyme-linked immunosorbent assay; PET, positron emission tomography; SUV, standardized uptake value; SUV_{Max}, maximum standardized uptake value; SUV_{Mean}, mean standardized uptake value; VOI, volume of interest.

Abstract

The domestic ferret (*Mustela putorius furo*) has been a long-standing animal model used in the evaluation and treatment of human diseases. Molecular imaging techniques such as 2-deoxy-2-(^{18}F)fluoro-D-glucose (^{18}F-FDG) positron emission tomography (PET) would be an invaluable method of tracking disease in vivo, but this technique has not been reported in the literature. Thus, the aim of this study was to establish baseline imaging characteristics of PET/computed tomography (CT) with ^{18}F-FDG in the ferret model. Twelve healthy female ferrets were anesthetized and underwent combined PET/CT scanning. After the images were fused, volumes of interest (VOIs) were generated in the liver, heart, thymus, and bilateral lung fields. For each VOI, standardized uptake values (SUVs) were calculated. Additional comparisons were made between radiotracer uptake periods (60, 90, and >90 minutes), intravenous and intraperitoneal injections of ^{18}F-FDG, and respiratory gated and ungated acquisitions. Pulmonary structures and the surrounding thoracic and upper abdominal anatomy were readily identified on the CT scans of all ferrets and were successfully fused with PET. VOIs were created in various tissues with the following SUV calculations: heart (maximum standardized uptake value [SUV_{Max}] 8.60, mean standardized uptake value [SUV_{Mean}] 5.42), thymus (SUV_{Max} 3.86, SUV_{Mean} 2.59), liver (SUV_{Max} 1.37, SUV_{Mean} 0.99), right lung (SUV_{Max} 0.92, SUV_{Mean} 0.56), and left lung (SUV_{Max} 0.88, SUV_{Mean} 0.51). Sixty- to 90-minute uptake periods were sufficient to separate tissues based on background SUV activity. No gross differences in image quality were seen between intraperitoneal and intravenous injections of ^{18}F-FDG. Respiratory gating also did not have a significant impact on image quality of lung parenchyma. The authors concluded that ^{18}F-FDG PET and CT imaging can be performed successfully in normal healthy ferrets with the parameters identified in this study. They obtained similar imaging features and uptake measurements with and without

respiratory gating as well as with intraperitoneal and intravenous ^{18}F-FDG injections. ^{18}F-FDG PET and CT can be a valuable resource for the in vivo tracking of disease progression in future studies that employ the ferret model.

Key Words: animal model; FDG-PET/CT; ferret; imaging; molecular imaging; pulmonary imaging; radiology; thoracic anatomy

Introduction

The development and study of animal models that reflect human disease have been a long-standing priority for drug and vaccine research in accordance with the US Food and Drug Administration regulatory requirements for preclinical trials (FDA 2002, 2009). Animal models of myocardial infarction, heart failure, chronic obstructive pulmonary disorder, and pulmonary infections all have resulted in advances toward uncovering pathogenesis and identifying novel treatments (Chimenti et al. 2004; Hasenfuss 1998; Ordway et al. 2008; Russell and Proctor 2006; van den Brand et al. 2010; Wright et al. 2008). The domestic ferret (*Mustela putorius furo*) has been used to study a variety of organ systems (Fox 1998). In the cardiovascular system, investigators have used ferrets to model acute thrombosis and myocardial hypertrophy (Baudet and Ventura-Clapier 1990; Schumacher et al. 1996). In the gastrointestinal system, ferrets have a documented susceptibility to infections such as *Campylobacter jejuni* and *Helicobacter pylori* (Chu et al. 2008; Kirkeby et al. 2009; Larin 1955; Lipatov et al. 2009; Maher and DeStefano 2004; Matsuoka et al. 2009; Reuman et al. 1989); and in the pulmonary system, the ferret has been useful as a model for obstructive conditions such as asthma (Kurucz and Szelenyi 2006) and cystic fibrosis (Fisher et al. 2011). Researchers have also used ferrets in evaluations of drugs that target human influenza virus (Baras et al. 2008; Boltz et al. 2008) and SARS coronavirus (Roberts et al. 2008; See et al. 2008).

Experimental designs using these models have traditionally required serial euthanasia at specified time points to assess pathologic changes. In vivo imaging techniques such as radiography and nuclear medicine have the potential to decrease the number of animals used, measure real-time responses in disease progression, and accelerate therapeutic discovery studies. A combination of positron emission tomography (PET[1]) and computed tomography (CT[1]), which fuses the molecular information of radiolabeled tracers at the subcellular level of PET with the cross-sectional anatomical information of CT, would give both spatial and temporal information on a single subject, allow each subject to serve as its own internal control, and possibly reduce the number of subjects needed for statistical significance. The most common PET imaging radiotracer used in clinical and basic science research is 2-deoxy-2-(^{18}F)fluoro-D-glucose (^{18}F-FDG[1]). The glycolytic rate of this analog of glucose serves as a measure of metabolic activity, which can be increased in pathophysiologic states such as malignancy, inflammation, and infection (Baum et al. 2010; Chen et al. 2009; Czernin et al. 2010; Kwee and Kwee 2009; Kwee et al. 2008; Love et al. 2009). In inflammation and infection, an increase in ^{18}F-FDG uptake is thought to be due to the presence of activated leukocytes (mostly neutrophils) in the tissue of interest (Chen and Schuster 2004; Goldsmith and Vallabhajosula 2009; Jones et al. 1994).

Because ^{18}F-FDG is used to measure metabolic activity, it can be employed in many of the models described above, particularly in the thoracic cavity. The ferret is an especially attractive model for pulmonary studies because its long trachea, large lung capacity, and bronchiolar branching facilitate radiographic analysis and histopathologic comparison. Inflammatory changes in diseases such as asthma and cystic fibrosis could be assessed with ^{18}F-FDG and followed during treatment protocols. ^{18}F-FDG could also be used to track activated leukocytes in pulmonary infections as well as any resulting inflammatory sequelae. Although ^{18}F-FDG PET/CT has been studied comprehensively in other models such as the mouse (Abbey et al. 2004; Deroose et al. 2007; Rowland and Cherry 2008; Shoghi et al. 2008; Virostko and Powers 2009), the results have not been reported in the literature of the ferret model at the time of this writing. The lack of imaging studies stands as a current impediment in basic and clinical science because clinicians commonly rely on chest radiography and CT to assess the severity of pulmonary disease and guide patient management. Certainly, the increasing use of molecular imaging methods such as PET to study the microbial pathogenesis in laboratory animals and humans can be translated to the ferret (Kalicke et al. 2000; Sathekge et al. 2010). Challenges to using ferrets in PET/CT include (1) unique body size dimensions that may not fit traditional preclinical PET/CT hardware, (2) thoracic anatomy not previously characterized in radiologic literature, (3) potentially unusual biodistribution of molecular radiotracers, (4) scarce data comparing imaging techniques, and (5) respiratory physiology that warrants specialized handling and imaging protocols to optimize data acquisition and avoid artifacts. These challenges led us to investigate the use of this baseline molecular imaging technique in the ferret model presented herein.

In this article, we explore the feasibility of imaging ferret thoracic anatomy by performing CT and PET imaging of uninfected animals. We used a standard PET/CT instrument with ^{18}F-FDG, the most commonly employed PET radiotracer. We focused on the following

areas of concern that affect the success of small animal imaging: (1) Establishment of normal thoracic anatomy by CT, (2) ^{18}F-FDG distribution and uptake by various organs, (3) efficient methods of image postprocessing and analysis, (4) consequence of radiotracer uptake period on signal:noise ratio, (5) comparison of intraperitoneal and intravenous injection of radiotracer, and (6) influence of respiratory gating on image quality. Our findings establish the parameters for PET/CT imaging of the thorax effectively in ferrets, suggesting that these techniques can greatly accelerate the study of lung diseases in this animal model.

Methods

Animals

Animal studies were conducted at the University of Louisville, which is accredited by the Association for Assessment and Accreditation of Laboratory Animal Care International, and were approved by the University of Louisville Institutional Animal Care and Use Committee. Animals received care in accordance with the *Guide for the Care and Use of Laboratory Animals* (NRC 2010) and the US Animal Welfare Regulations. We obtained female ferrets between 26 and 28 weeks of age, weighing 600 to 1000 g each, from Triple F Farms (Sayre, PA). The vendor ovariohysterectomized, descented, and tattooed the ferrets for identification before shipment. The animals were housed in pairs within stainless steel ventilated caging with slotted flooring (24″ W × 31″ D × 16″H) in a temperature- (20.0-22.2ºC) and humidity- (30%-70%) controlled room on a 12:12 hour light:dark cycle. Animal Biosafety Level 2 practices were employed. Cage pans below the slotted flooring were lined with Techboard K52 (Shepherd Specialty Papers Inc., Watertown, TN), and cages and racks were sanitized twice weekly. The ferrets were acclimated for 7 days before initiation of the study and were fed Teklad Laboratory Diet #2072 (Harlan/Teklad, Madison, WI) ad libitum. Staff provided tap water ad libitum via water bottle along with environmental enrichment in the form of a nesting box filled with paper nesting material (Enviro-dri®, Shepherd Specialty Papers Inc., Watertown, TN), cotton ferret beds and sleeper sacks (Feeder's Supply, Louisville, KY), and toys (Jingle Balls™ and Dumbbells, Bio-Serve®, Frenchtown, NJ).

Vendor microbiological monitoring reports indicated that the ferrets were serologically negative for Aleutian disease virus by enzyme-linked immunosorbent assay (ELISA[1]) as well as other infectious organisms including *Streptococcus*, *Klebsiella*, and *Staphylococcus* species. In addition, animals were vaccinated against canine distemper virus and were treated with ivermectin by the vendor before shipping. Ferret blood samples were sent to the University of Louisville for screening for antibodies against influenza A 2009 pandemic H1N1 and seasonal H1N1 and H3N2 viruses by both ELISA and hemagglutination inhibition assays. On arrival to our facility, fecal specimens of representative animals were examined and were negative for intestinal parasites.

For all procedures, animals were anesthetized with 3 to 5% isoflurane in an induction chamber, intubated with 2.0 Fr endotracheal tubes, and maintained under anesthesia with 1 to 3% isoflurane. All animals were fasted 3 to 4 hours before anesthesia to prevent aspiration of gastrointestinal contents. Serum blood glucose levels were checked with a commercial glucometer (Freestyle Lite®, Abbott Laboratories, Abbott, IL) before the induction of anesthesia and upon completion of imaging to ensure that animals were not hypoglycemic. During anesthesia and imaging, body temperature was supported with supplemental heat sources, and Artificial Tears Ophthalmic Ointment (Butler Schein Animal Health, Dublin, OH) was applied to the surface of the eyes to prevent corneal drying and ulceration. Animals were monitored continuously during anesthesia and imaging until they were fully recovered.

CT Imaging

We performed imaging studies with a Siemens Inveon Trimodal Scanner (Siemens Preclinical, Knoxville, TN), which is a small animal imaging platform that combines PET and CT modalities within one unit. This combination facilitated coregistration of PET and CT images inasmuch as the study subject was kept in a uniform position on the scanner bed, minimizing potentially large motion artifacts as a result of repositioning the animal between each scan. The Inveon CT scanner features a variable-focus tungsten X-ray source with an achievable resolution of 20 μm and a detector with a maximum field of view of 8.4 cm × 5.5 cm. The source-to-object distance was 263.24 mm, and the source-to-detector distance was 335.67 mm. The Inveon PET detector provided an axial field of view of 12.7 cm with a spatial resolution of 1.8 mm. We reconstructed PET images using a two-dimensional filtered backprojection algorithm with attenuation correction provided by CT imaging. For the CT scan, we used the following imaging settings: two bed positions, 80 kVp, 500 μA, 500 ms exposure time, 0.21 mm^3 voxels, 4 × 4 binning, with and without respiratory gating. We initiated gating after a default delay during the exhalation phase of each respiratory cycle as soon as a user-defined threshold detection had been triggered. We then acquired CT imaging for 100 msec at a given projection and continued for four subsequent triggerable

events. We repeated the entire process for all remaining CT projections.

PET Imaging

After each ferret underwent CT imaging, we reset the bed position, and the animal subsequently underwent PET imaging with ^{18}F-FDG (PETNET, Knoxville, TN). We checked blood glucose levels before administering radiolabeled tracer to ensure that they were within normal limits (62-134 mg/dL) (Quesenberry and Rosenthal 2003). We then performed PET imaging of animals at 60, 90, and >90 minute intervals. We did not perform dynamic imaging in this study in an effort to maximize animal care outside the scanner during the uptake intervals. We made additional comparisons between intravenous (via a 22- to 26-G catheter inserted into the cephalic vein) and intraperitoneal administration of ^{18}F-FDG. To maximize photon counts (sensitivity), each animal received the maximum allowable dose for the detector in this imaging platform, which was 74 to 123 MBq/kg of ^{18}F-FDG.

Image Analysis

We processed all imaging data with PMOD software (v3.1; PMOD Technologies Ltd., Zurich, Switzerland). We received CT data from the Inveon platform as Digital Imaging and Communications in Medicine (DICOM) files and PET data as MicroPET files. Scans were imported into the local database of the program with the units for the PET radiotracer in kBq/cc. We coregistered PET images with the CT images and resliced as necessary to facilitate later calculations. For analysis of ^{18}F-FDG activity, we used the standardized uptake value (SUV[1]). SUV is a widely used semiquantitative measure that normalizes radiotracer uptake in a given region of interest based on body weight. The calculation for this study appears below:

$$\mathrm{SUV} = \frac{\text{Tissue Radioactivity Concentration (kBq/mL)}}{\text{Injected FDG Dose (kBq)}} * \text{Body Weight (g)}$$

Equation 1

For all calculations, we expressed animal weights in kilograms and FDG activity in megabecquerels. For each image series, we calculated SUVs for each voxel using PMOD, with the radionuclide half-life set at 6586.2 sec for ^{18}F-FDG.

For each imaging series, we used CT scans for gross localization of organs and placement of a volume of interest (VOI[1]) for any given region. We programmatically generated a sphere for the liver using PMOD by specifying a radius of 2.0 mm in the left hepatic lobe in a representative area of homogeneity, and we were careful to avoid the photopenic gallbladder. We used a similar approach to identify the background activity of the lungs, with spherical VOIs of 1.5-2 mm radius generated in areas of the lung having visually uniform activity. For other visualized organs such as the heart and thymus, we utilized a semiautomated approach. For the cardiac structures, we constructed an ellipsoid that encompassed both atria and ventricles, and we then used automatic isocontour detection to refit the VOI around the structures by setting a threshold of 50 to 60% of the difference between the maximum and minimum intensity SUVs in the ellipsoid VOI, as shown below:

$$0.50 * (\mathrm{SUV_{Max}} - \mathrm{SUV_{Min}})$$

Equation 2

$$0.60 * (\mathrm{SUV_{Max}} - \mathrm{SUV_{Min}})$$

Equation 3

We used a similar method to isolate the thymus. In cases where the automated thresholding included contiguous structures in the VOI, we used manual refitting in conjunction with the coregistered CT scan to exclude those surrounding structures. For all VOIs, we calculated maximum SUV ($\mathrm{SUV_{Max}}$[1]) and calculated average and standard deviation of all pixels in the volume (mean standardized uptake value [$\mathrm{SUV_{Mean}}$[1]] ± standard deviation).

Results

Twelve 4- to 6-month-old female ferrets were included in the study. After successful anesthesia and intubation, the ferrets were placed on the scanning bed. Initial CT scans were performed to identify prominent structures in normal ferret pulmonary anatomy (Figure 1). In the right lung, the ferret has an upper (cranial) lobe, a middle lobe, a lower (caudal) lobe, and an accessory lobe in the

medial lung base. In the left lung, there is an upper (cranial) and a lower (caudal) lobe (Fox 1998). We used soft tissue windowing to identify vascular, mediastinal, and muscular structures in the ferret (Figure 2). Using the CT settings outlined previously, the superior vena cava, inferior cava, and aorta were readily identifiable and traceable in three projections (sagittal, coronal, and transaxial).

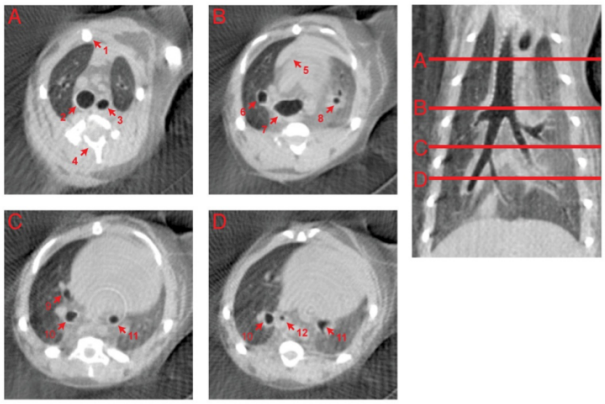

Figure 1. Anatomical structures on computed tomography (lung windowing). Axial sections (left, A-D) and coronal section with red localizing bars (right). Anatomical structures labeled with numbered arrows: (1) sternebra, (2) trachea, (3) esophagus, (4) thoracic vertebra, (5) thymus, (6) bronchus to right cranial lobe, (7) tracheal carina, (8) bronchus to left cranial lobe, (9) bronchus to right middle lobe, (10) bronchus to right caudal lobe, (11) bronchus to left caudal lobe, (12) bronchus to right accessory lobe.

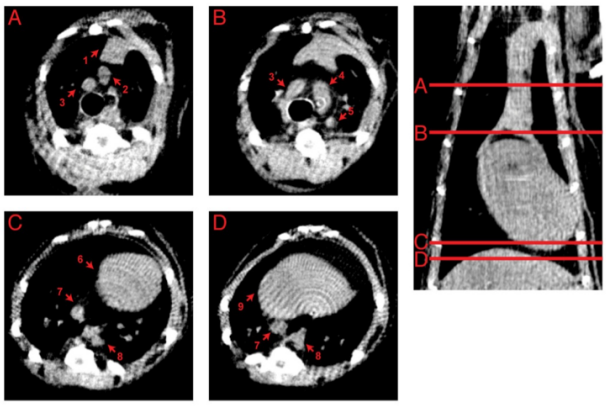

Figure 2. Anatomical structures on computed tomography (soft tissue windowing). Axial sections (left, A-D) and coronal section with red localizing bars (right). Anatomical structures labeled with numbered arrows: (1) thymus, (2) lymph node, (3) superior vena cava, (4) Aortic arch, (5) Lymph node, (6) Heart, (7) Inferior vena cava, (8) descending aorta, (9) Liver.

For each ferret, we performed, coregistered, and fused PET imaging with corresponding CT scans (Figure 3). Areas of mildly increased ^{18}F-FDG uptake were noted in the thymus, subcarinal, and paratracheal lymph nodes. Intense uptake, as expected, was in the myocardium. In the lung parenchyma, we noted no focal areas of consolidation or opacification on CT , and we identified no analogous metabolically active regions on PET.

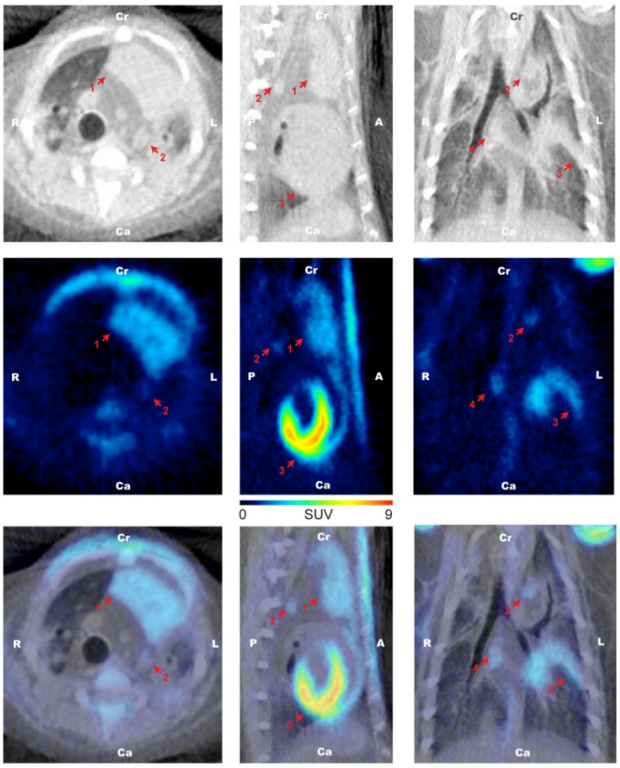

Figure 3. Metabolically active structures as seen on fused 18F-FDG PET/CT images. Axial sections (left column), sagittal sections (middle column), coronal sections (right column). Computed tomography (top row), positron emission tomography (middle row), and fusion (bottom row) after 90-minute uptake. Anatomical structures labeled with numbered arrows: (1) thymus, (2) paratracheal lymph node, (3) myocardium, (4) subcarinal lymph node. 18F-FDG, 2-deoxy-2-(18F)fluoro-D-glucose. Orientation: A, anterior; P, posterior. R, right; L, left; Cr, cranial; Ca, caudal.

We created volumetric constructions to delineate regions of interest in PET scans (Figure 4). To calculate ^{18}F-FDG activity, we used PMOD to create generalized ellipsoid and cuboid VOIs in the heart and thymus, respectively. We then refitted the VOIs to the structures using previously described methods (Equations 2 and 3). For the liver and the lungs, spherical VOIs were sufficient to calculate background activity. In a few cases, automatic refitting would erroneously include surrounding structures with elevated ^{18}F-FDG activity, which we manually removed. We obtained average values for all ferrets included in the study (Table 1). The heart had the highest uptake values with an average SUV_{Max} of 8.60 and SUV_{Mean} of 5.42. The thymus was the second most metabolically active organ, followed by the liver. The right and left lungs showed reasonable symmetric values with expectedly low intensities compared with other tissues: SUV_{Max} of 0.92 and 0.88, and SUV_{Mean} of 0.56 and 0.51, respectively.

Table 1 Normal values for SUV_{Max} and SUV_{Mean} of tissues in the ferret*

	SUV_{Max}	**SUV_{Mean}**
Heart	8.60 ± 3.66	5.42 ± 2.31
Thymus	3.86 ± 1.25	2.59 ± 0.85
Liver	1.37 ± 0.54	0.99 ± 0.46
R. Lung	0.92 ± 0.18	0.56 ± 0.20

L. Lung	0.88 ± 0.25	0.51 ± 0.21

***Values are listed with respective standard deviations. SUV, standardized uptake value.**

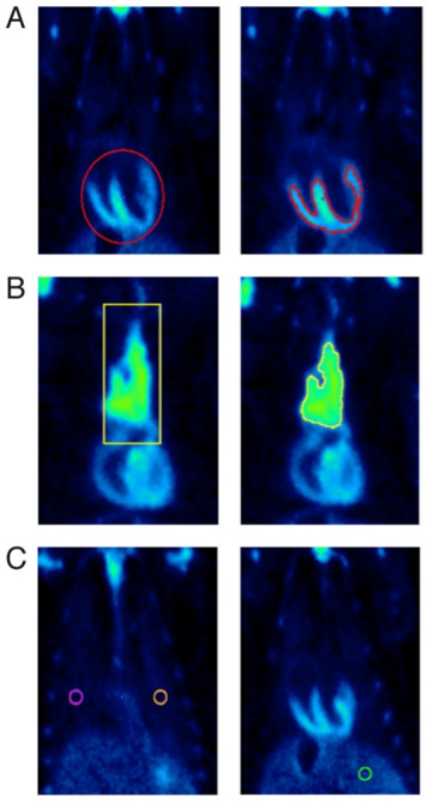

Figure 4. VOI generation in tissues using PMOD software. A) An ellipsoid VOI surrounding the heart was refitted using a 50% threshold difference. B) A rectangular prism VOI encompassing the thymus was refitted using a 50% threshold difference. C) Spherical VOIs in the right lung (pink), left lung (orange), and liver (green). VOI, volume of interest.

We performed a number of technique trials to ascertain their effect on imaging quality. First, in human subjects, the uptake period for ^{18}F-FDG is usually around 60 minutes for optimal signal:noise ratio. Because the ideal uptake period is unknown in ferrets, we assessed the optimal timing between radiotracer administration and initiation of PET imaging by grouping uptake phases at 60 minutes (n = 5), 90 minutes (n = 4), and > 90 minutes (average 110 minutes, n = 3) (Figure 5). As previously noted, we did not perform dynamic imaging in an effort to maximize animal care outside the scanner during the uptake periods. We obtained SUV_{Mean} values from VOIs in the liver, heart, thymus, and bilateral lung fields as described previously. In each uptake period, the heart had the consistently highest SUV_{Mean}, followed by the thymus and liver. The right and left lungs had values similar to each other for all uptake durations, with intensities appropriately lower than other tissues at the 60- and 90-minute uptake periods. By >90 minutes, it was more difficult to distinguish the SUV_{Mean} of the lungs from the liver due to decreasing liver intensity.

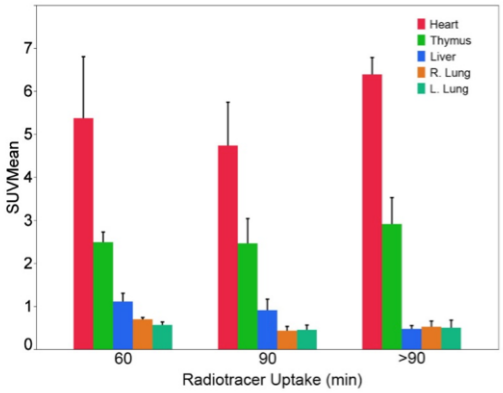

Figure 5. Mean standardized uptake value (SUVmean) for tissues based on radiotracer uptake period of 2-deoxy-2-(18F)fluoro-D-glucose (18F-FDG).

Because it is also unknown which administration method of ^{18}F-FDG is optimal, we compared PET images acquired after intravenous (n = 6) and intraperitoneal injections (n=6) of ^{18}F-FDG at an uptake period of 90 minutes (Figure 6). The route of administration did not affect the ability to align and fuse the PET and CT scans. The heart was the most metabolically active in both routes, followed by the thymus and liver. Overall, the trend in both administration routes demonstrated that the right and left lungs were the least metabolically active, as expected. Regardless of method, we observed no focal areas of increased ^{18}F-FDG uptake in the lung parenchyma on visual comparison.

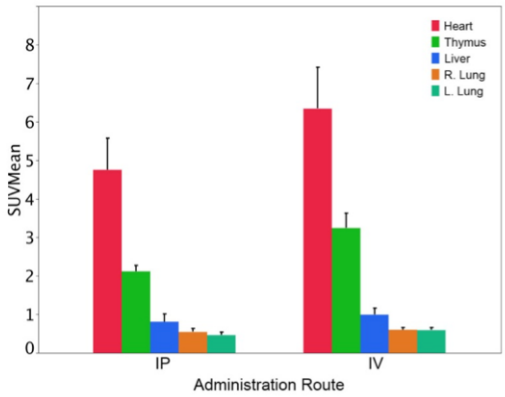

Figure 6. Mean standardized uptake value (SUVmean) of tissues based on administration route of 2-deoxy-2-(18F)fluoro-D-glucose. IP, intraperitoneal. IV, intravenous.

Finally, we used respiratory gating to assess differences in CT image quality (Figure 7). Respiratory gating involves the acquisition of photon events at specific points during periods of the respiratory cycle, such as during maximal inspiration by the subject, in order to reduce motion artifact, keep specific lesions in roughly the same position, and increase overall spatial resolution. Similar to other comparisons, respiratory gating did not detract or enhance from our ability to coregister CT and PET images. In addition, we could readily fuse the images using PMOD. Visually, in the absence of lesions, there was no substantial difference in imaging features compared with ungated acquisitions. In both gated and ungated images, soft tissue structures such as the heart and liver were readily distinguishable from the lung parenchyma.

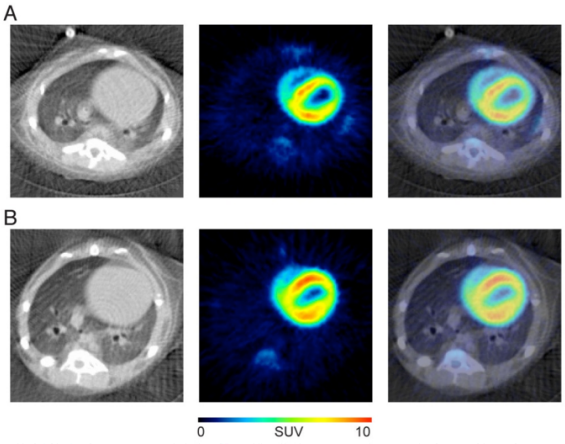

Figure 7. Comparison of computed tomography(CT), positron emission tomography (PET), and fusion images using respiratory gating. A) ungated, B) gated. No gross differences are noted in image resolution, anatomic localization, or fusion image.

Discussion

In this study, we have demonstrated a technique for obtaining CT and PET images in anesthetized ferrets. The ferret has been successfully employed in the study of several respiratory pathogens, and with the ferret genome near completion, it has great potential for increased use in the study of human pulmonary disease processes. Herein we establish a ^{18}F-FDG PET/CT imaging technique that could be valuable in future efforts. To that end, we believed it was important to describe anatomical features on PET and CT and to compare technical strategies for imaging. We thus identified normal ferret anatomy in our study on CT scans in both lung and soft tissue windows, and this information facilitated later identification of pertinent structures on the PET scan for localizing ^{18}F-FDG uptake. The anatomical characterization is intended to inform future investigators regarding the features of ferret anatomy that differ from human, such as the ferret's right accessory caudal lobe. Although the image quality was sufficient for the purposes of this study, future studies could incorporate projections at finer increments to increase resolution.

Overall, the long thoracic anatomy of the ferret may provide productive avenues for pulmonary disease research using imaging for in vivo measurement. Lymph nodes, which were well characterized (Figure 3), can be useful for future studies of neoplastic, infectious, and inflammatory conditions. Myocardial uptake was also well demonstrated in this study, suggesting that ^{18}F-FDG PET/CT may contribute to the range of cardiac research using the ferret model (Dudas-Gyorki et al. 2011; Gomoll 1996; Klabunde and Mulligan 1998; Poucher et al. 1994).

We demonstrated automated and semiautomated methods of generating VOIs in tissues of interest. To measure background activity in a larger organ such as the liver or lobes of the lung, programmatically generated spherical VOIs with a 2.0 mm radius were sufficient to calculate SUV statistics. For more irregular structures such as the myocardium or thymus, an initially generic ellipsoid or rectangular prism could be adequately refitted to the target organ using appropriate thresholds (Equations 2 and 3). Of note, it is imperative for the researcher to scan through individual slices (or look on a 3D locator) to ensure that adjacent structures of similar or increased SUV values are not accidentally included in the VOI. Failure to do so could result in the erroneous inclusion of much more metabolically active structures into calculations, which could skew uptake measurements such as SUV_{Max} and SUV_{Mean}.

The importance of measuring optimal uptake time periods cannot be overstated in planning a animal research study because different uptake periods greatly affect animal management, imaging workflow, fasting periods, and the number of subjects imaged on any given day. We assessed the timing between administration of the radiotracer and initiation of PET imaging at 60, 90, and >90 minutes. Our study shows that high-quality imaging can be achieved using an uptake period of 60 to 90 minutes, whereas longer periods may cause the radiotracer to wash out of the liver, making it more difficult to distinguish from the adjacent lung parenchyma. Because the background SUVs in the lungs was lower than all other tissues, even at shorter uptake periods, we determined that a 60- to 90-minute period was sufficient to allow enough of the radiotracer to accumulate in tissues of interest and to assist in discriminating between the various organs.

The choice of whether to use an intravenous or intraperitoneal route of radiotracer administration is important because either strategy demands certain technical skill and resources, in addition to having an impact on the resource planning and workflow of any experiment. Thus, it was essential to compare both routes to assess for differences in ^{18}F-FDG PET/CT image production. In our study, coregistration of PET and CT imaging using both routes was equally feasible, and they both yielded similar SUV calculations.

We had anticipated that a high ratio of cranial-caudal length to axial diameter of the lungs, in addition to an elevated respiratory rate, would be a significant limiting factor for image quality. Consequently, we compared respiratory gated with nonrespiratory gated PET/CT techniques. Our comparison did not yield large differences in image quality for visual assessment of lung parenchyma or a significant impact on image count statistics. Perhaps due to the fact that the respiratory rate for a ferret typically ranges from 30 to 40 breaths per minute and that we used a 500-ms acquisition time, there may not have been sufficient movement during respiration to require respiratory gating. However, it is important to note that our experiment did not assess differences in detecting and localizing subcentimeter lesions such as lung nodules.

The calculation of SUV is an important methodological issue in clinical and preclinical PET research. Due to the variability in human habitus and fat composition, it is widely advocated that lean body mass be the adjustment for SUV calculations. Our study uses total body weight for several reasons: 1) Ferrets in this study were controlled for weight, age, and gender; 2) exact measurements of fat composition in ferrets is unknown; and 3) other small animal PET/CT studies routinely employ total body weight in SUV calculations (Paproski et al. 2010; Walter et al. 2010). It is possible for future studies to use lean body mass adjustments when greater variability in the animal subjects is present.

Our study has several limitations. First, some of our technique comparisons were limited by smaller sample sizes. Second, we used an imaging platform that was originally designed for rodents such as mice and rats, and certain methodologies had to be adapted, as described earlier. It is possible that future PET/CT configurations will be better suited for this animal model's size dimensions. Third, the study primarily focuses on thoracic structures with partial imaging of the upper abdomen. This thoracic emphasis was reasonable due to the ferret's long thoracic anatomy, which provides more anatomical and physiologic detail. We included portions of the liver in the reported data. We did not report splenic imaging data because the spleen is located more caudally in the ferret and therefore was outside the field of view. Finally, we used a threshold of 50 to 60% in determining structural VOIs because this approach is commonly used in the literature (Krak et al. 2005; van Heijl et al. 2010; Weber et al. 1999). Nevertheless, varying the threshold can have a material impact on the assessment of calculations such as mean SUV. Thus future studies could be done to assess different percentages of thresholds on SUV measurements.

Having demonstrated proof of concept using combination PET/CT imaging in ferrets at baseline, we envision future studies to include ferrets challenged with inflammatory factors such as lipopolysaccharide and infectious agents such as H1N1 influenza. Ferrets are an ideal model for influenza studies compared with more commonly used models such as mice and nonhuman primates (Bodewes et al. 2010). As noted previously, one of the more important considerations is the fact that ferrets are permissive hosts for the influenza virus, which means that the virus does not typically have to be adapted to the animal to infect, more closely mimicking the infectious agent in humans. In the case of mice and rats, the human seasonal influenza virus requires adaptation before it can replicate in the animal and cause disease. In addition, ferrets display signs and symptoms of severe influenza infection similar to humans, which helps to assess susceptibility to the infection and pathophysiologic comparability to human hosts. In contrast, mice do not typically show outward signs of fever after infection. Furthermore, the size, disposition, and maintenance of ferrets make them more desirable ass models than other large animals such as nonhuman primates for the study of infectious disease.

We also demonstrate the potential utility of PET for cardiac research and lymph nodal disease. Although we have demonstrated radiotracer uptake at specific time points, we believe that future studies incorporating dynamic acquisitions would be helpful to characterize the ideal time points for imaging. We did not perform such analyses in this pilot study due to the necessity of safeguarding the health of the ferret, the extensive periods that the ferret would need to be in the scanner, and the complexities of performing such studies in a BSL-3 environment. Based on the images obtained in this study (Figure 2), it would be feasible to draw ROIs around major vascular structures such as the aorta in order to derive input functions for kinetic analyses. It would also be possible to incorporate biodistrubtion studies and autoradiography into future work for more quantitative measurements of radiotracer activity and localization.

We hypothesize that PET imaging would be an extremely useful modality that would provide in vivo tracking of inflammation and infection in the ferret model. The semiautomated approach we used for VOI generation could be used to isolate regions of

consolidation or inflammation in the lung that showed increased ^{18}F-FDG uptake on PET scan. Further attempts could also be made to increase the resolution of the CT scans and help to identify smaller and potentially more diseased regions of the lungs. In addition, while we presented a number of values by which PET scans could be semiquantitatively tracked, correlation of imaging features with advancing disease processes on pathology and microbiology would provide validations of measurement techniques.

Conclusion

We developed a method for imaging anesthetized ferrets using ^{18}F-FDG PET/ CT. We demonstrated a semiautomated method for evaluating regions of interest as well as performing SUV calculations of those regions. These values serve as important baseline standards in the healthy ferret. We also compared various imaging techniques and demonstrated SUV trends in most thoracic and upper abdominal tissues with increasing radiotracer uptake periods. We identified similar SUV distributions and intensities in comparisons of intravenous versus intraperitoneal injections of ^{18}F-FDG in most tissues. Uptake periods ranging from 30 to 90 minutes are feasible and may be optimized to workflow constraints. The 60-minute uptake period produced high-quality imaging and matches the uptake period used in human clinical imaging. Respiratory gating was not required to provide sufficient visual discrimination of anatomical structures and fusion with PET images.

Our study supports the conclusion that ^{18}F-FDG PET/CT is technically feasible in the ferret model. We believe that this imaging modality could make a significant contribution to future preclinical and translational studies tracking in vivo disease.

Acknowledgments: This study was supported in part by the Commonwealth of Kentucky-funded Clinical and Translational Science Pilot Project Program at the University of Louisville, the Clinical Research Training Program (a public-private partnership supported jointly by the National Institutes of Health (NIH) and Pfizer Inc. via a grant to the Foundation for NIH from Pfizer Inc.), and the Center for Infectious Disease Imaging in the Intramural Research Program of NIH.

References

Abbey CK, Borowsky AD, McGoldrick ET, Gregg JP, Maglione JE, Cardiff RD, Cherry SR. 2004. In vivo positron-emission tomography imaging of progression and transformation in a mouse model of mammary neoplasia. Proc Natl Acad Sci U S A 101:11438-11443.

Baras B, Stittelaar KJ, Simon JH, Thoolen RJ, Mossman SP, Pistoor FH, van Amerongen G, Wettendorff MA, Hanon E, Osterhaus AD. 2008. Cross-protection against lethal H5N1 challenge in ferrets with an adjuvanted pandemic influenza vaccine. PLoS One 3:1401.

Baudet S, Ventura-Clapier R. 1990. Differential effects of caffeine on skinned fibers from control and hypertrophied ferret hearts. Am J Physiol 259:1803-1808.

Baum RP, Swietaszczyk C, Prasad V. 2010. FDG-PET/CT in lung cancer: An update. Front Radiat Ther Oncol 42:15-45.

Bodewes R, Rimmelzwaan GF, Osterhaus AD. 2010. Animal models for the preclinical evaluation of candidate influenza vaccines. Expert Rev Vaccines 9:59-72.

Boltz DA, Rehg JE, McClaren J, Webster RG, Govorkova EA. 2008. Oseltamivir prophylactic regimens prevent H5N1 influenza morbidity and mortality in a ferret model. J Infect Dis 197:1315-1323.

Chen DL, Bedient TJ, Kozlowski J, Rosenbluth DB, Isakow W, Ferkol TW, Thomas B, Mintun MA, Schuster DP, Walter MJ. 2009. [18F]Fluorodeoxyglucose positron emission tomography for lung antiinflammatory response evaluation. Am J Respir Crit Care Med 180:533-539.

Chen DL, Schuster DP. 2004. Positron emission tomography with [18F]fluorodeoxyglucose to evaluate neutrophil kinetics during acute lung injury. Am J Physiol Lung Cell Mol Physiol 286:834-840.

Chimenti S, Carlo E, Masson S, Bai A, Latini R. 2004. Myocardial infarction: Animal models. Methods Mol Med 98:217-226.

Chu YK, Ali GD, Jia F, Li Q, Kelvin D, Couch RC, Harrod KS, Hutt JA, Cameron C, Weiss SR, Jonsson CB. 2008. The SARS-CoV ferret model in an infection-challenge study. Virology 374:151-163.

Czernin J, Benz MR, Allen-Auerbach MS. 2010. PET/CT imaging: The incremental value of assessing the glucose metabolic phenotype and the structure of cancers in a single examination. Eur J Radiol 73:470-480.

Deroose CM, De A, Loening AM, Chow PL, Ray P, Chatziioannou AF, Gambhir SS. 2007. Multimodality imaging of tumor xenografts and metastases in mice with combined small-animal PET, small-animal CT, and bioluminescence imaging. J Nucl Med 48:295-303.

Dudas-Gyorki Z, Szabo Z, Manczur F, Voros K. 2011. Echocardiographic and electrocardiographic examination of clinically healthy, conscious ferrets. J Small Anim Pract 52:18-25.

FDA [Food and Drug Administration]. 2002. New drug and biological drug products: Evidence needed to demonstrate effectiveness of new drugs when human efficacy studies are not ethical or feasible. Final rule. Fed Regist 67:37988-37998.

FDA [Food and Drug Administration]. 2009. Guidance for Industry: Animal Models — Essential Elements to Address Efficacy Under the Animal Rule In:Services USDoHaH, ed. Silver Spring: FDA. pp 1-19.

Fisher JT, Zhang Y, Engelhardt JF. 2011. Comparative biology of cystic fibrosis animal models. Methods Mol Biol 742:311-334.

Fox JG. 1998. Biology and Diseases of the Ferret. Baltimore: Lippincott Williams & Wilkins.

Goldsmith SJ, Vallabhajosula S. 2009. Clinically proven radiopharmaceuticals for infection imaging: Mechanisms and applications. Semin Nucl Med 39:2-10.

Gomoll AW. 1996. Cardioprotection associated with preconditioning in the anesthetized ferret. Basic Res Cardiol 91:433-443.

Hasenfuss G. 1998. Animal models of human cardiovascular disease, heart failure and hypertrophy. Cardiovasc Res 39:60-76.

Jones HA, Clark RJ, Rhodes CG, Schofield JB, Krausz T, Haslett C. 1994. In vivo measurement of neutrophil activity in experimental lung inflammation. Am J Respir Crit Care Med 149:1635-1639.

Kalicke T, Schmitz A, Risse JH, Arens S, Keller E, Hansis M, Schmitt O, Biersack HJ, Grunwald F. 2000. Fluorine-18 fluorodeoxyglucose PET in infectious bone diseases: Results of histologically confirmed cases. Eur J Nucl Med 27:524-528.

Kirkeby S, Martel CJ, Aasted B. 2009. Infection with human H1N1 influenza virus affects the expression of sialic acids of metaplastic mucous cells in the ferret airways. Virus Res 144:225-32.

Klabunde RE, Mulligan LJ. 1998. The ferret as a model for myocardial infarct size reduction by use of a selectin inhibitor. Lab Anim Sci 48:529-532.

Krak N, Boellaard R, Hoekstra OS, Twisk JWR, Hoekstra CJ, Lammertsma AA. 2005. Effects of ROI definition and reconstruction method on quantitative outcome and applicability in a response monitoring trial. Eur J Nucl Med Mol Imaging 32:294–301.

Kurucz I, Szelenyi I. 2006. Current animal models of bronchial asthma. Current Pharmaceut Des 12:3175-3194.

Kwee TC, Kwee RM. 2009. Combined FDG-PET/CT for the detection of unknown primary tumors: Systematic review and meta-analysis. Eur Radiol 19:731-744.

Kwee TC, Kwee RM, Alavi A. 2008. FDG-PET for diagnosing prosthetic joint infection: Systematic review and meta-analysis. Eur J Nucl Med Mol Imaging 35:2122-2132.

Larin NM. 1955. Canine distemper virus in the ferret. J Comp Pathol 65:325-333.

Lipatov AS, Kwon YK, Pantin-Jackwood MJ, Swayne DE. 2009. Pathogenesis of H5N1 influenza virus infections in mice and ferret

models differs according to respiratory tract or digestive system exposure. J Infect Dis 199:717-725.

Love C, Marwin SE, Palestro CJ. 2009. Nuclear medicine and the infected joint replacement. Semin Nucl Med 39:66-78.

Maher JA, DeStefano J. 2004. The ferret: An animal model to study influenza virus. Lab Anim (NY) 33:50-53.

Matsuoka Y, Lamirande EW, Subbarao K. 2009. The ferret model for influenza. Curr Protoc Microbiol 13:15G.2.1–15G.2.29.

NRC [National Research Council]. 2010. Guide for the Care and Use of Laboratory Animals. 8th ed. Washington, DC: National Academy Press.

Ordway D, Henao-Tamayo M, Smith E, Shanley C, Harton M, Troudt J, Bai X, Basaraba RJ, Orme IM, Chan ED. 2008. Animal model of *Mycobacterium abscessus* lung infection. J Leuk Biol 83:1502-1511.

Paproski RJ, Wuest M, Jans HS, Graham K, Gati WP, McQuarrie S, McEwan A, Mercer J, Young JD, Cass CE. 2010. Biodistribution and uptake of 3′-deoxy-3′-fluorothymidine in ENT1-knockout mice and in an ENT1-knockdown tumor model. J Nucl Med 51:1447-1455.

Poucher SM, Brooks R, Pleeth RM, Conant AR, Collis MG. 1994. Myocardial infarction and purine transport inhibition in anaesthetised ferrets. Eur J Pharmacol 252:19-27.

Quesenberry KE, Rosenthal KL. 2003. Endocrine diseases. In: Quesenberry KE, Carpenter JW, eds. Ferrets, Rabbits, and Rodents: Clinical Medicine and Surgery. St. Louis: Saunders. pp 77-90.

Reuman PD, Keely S, Schiff GM. 1989. Assessment of signs of influenza illness in the ferret model. J Virol Methods 24:27-34.

Roberts A, Lamirande EW, Vogel L, Jackson JP, Paddock CD, Guarner J, Zaki SR, Sheahan T, Baric R, Subbarao K. 2008. Animal models and vaccines for SARS-CoV infection. Virus Res 133:20-32.

Rowland DJ, Cherry SR. 2008. Small-animal preclinical nuclear medicine instrumentation and methodology. Semin Nucl Med 38:209-222.

Russell JC, Proctor SD. 2006. Small animal models of cardiovascular disease: Tools for the study of the roles of metabolic syndrome, dyslipidemia, and atherosclerosis. Cardiovascpathology 15:318-330.

Sathekge M, Maes A, Kgomo M, Stoltz A, Pottel H, Van de Wiele C. 2010. Impact of FDG PET on the management of TBC treatment: A pilot study. Nuklearmedizin 49:35-40.

Schumacher WA, Steinbacher TE, Megill JR, Durham SK. 1996. A ferret model of electrical-induction of arterial thrombosis that is sensitive to aspirin. J Pharmacol Toxicol Methods 35:3-10.

See RH, Petric M, Lawrence DJ, Mok CP, Rowe T, Zitzow LA, Karunakaran KP, Voss TG, Brunham RC, Gauldie J, Finlay BB, Roper RL. 2008. Severe acute respiratory syndrome vaccine efficacy in ferrets: Whole killed virus and adenovirus-vectored vaccines. J Gen Virol 89:2136-2146.

Shoghi KI, Gropler RJ, Sharp T, Herrero P, Fettig N, Su Y, Mitra MS, Kovacs A, Finck BN, Welch MJ. 2008. Time course of alterations in myocardial glucose utilization in the Zucker diabetic fatty rat with correlation to gene expression of glucose transporters: A small-animal PET investigation. J Nucl Med 49:1320-1327.

van den Brand JM, Stittelaar KJ, van Amerongen G, Rimmelzwaan GF, Simon J, de Wit E, Munster V, Bestebroer T, Fouchier RA, Kuiken T, Osterhaus AD. 2010. Severity of pneumonia due to new H1N1 influenza virus in ferrets is intermediate between that due to seasonal H1N1 virus and highly pathogenic avian influenza H5N1 virus. J Infect Dis 201:993-999.

van Heijl M, Omloo JM, van Berge Henegouwen MI, van Lanschot JJ, Sloof GW, Boellaard R. 2010. Influence of ROI definition, partial volume correction and SUV normalization on SUV-survival correlation in oesophageal cancer. Nucl Med Commun 31:652-658.

Virostko J, Powers AC. 2009. Molecular imaging of the pancreas in small animal models. Gastroenterology 136:407-409.

Walter MA, Hildebrandt IJ, Hacke K, Kesner AL, Kelly O, Lawson GW, Phelps ME, Czernin J, Weber WA, Schiestl RH. 2010. Small-animal PET/CT for monitoring the development and response to chemotherapy of thymic lymphoma in Trp53-/- mice. J Nucl Med 51:1285-1292.

Weber WA, Ziegler SI, Thodtmann R, Hanasuke AR, Schwaiger M. 1999. Reproducibility of metabolic measurements in malignant tumours using FDG PET. J Nucl Med 40:1771–1777.

Wright JL, Cosio M, Churg A. 2008. Animal models of chronic obstructive pulmonary disease. Am J Physiol Lung Cell Molec Physiol 295:L1-L15.